Ammonia decomposition over iron-based catalyst: Exploring the hidden active phase

Bin Lu [a], Ling Li [b], Menghao Ren [a], Yu Liu [a], Yanmin Zhang [a], Xin Xu [a], Xuan Wang [a], Hengshan Qiu [a,*]

[a] *Engineering Research Center of Advanced Functional Material Manufacturing of Ministry of Education, School of Chemical Engineering, Zhengzhou University, Zhengzhou 450001, China*
[b] *Laboratory Management Center, Zhengzhou University, Zhengzhou 450001, China*

A B S T R A C T

The possible phase transformation of catalysts under reaction conditions brings lots of difficulties in establishing the active phase. Herein, we report a hidden active phase over iron catalyst uniquely for the dehydrogenation of ammonia (NH_3). The highest dehydrogenation rate corresponds to an evanescent Fe/Fe_4N mixing phase while the nitrogen (N) kept on accumulating and gradually deactivated the catalyst. Density functional theory (DFT) calculations demonstrated that deposition of an N on Fe(100) surface modifies the electronic structure of its surrounding iron atoms, causing a significant reduction of the initial dehydrogenation barrier of NH_3. To recover the hidden active phase, ambient-pressure double dielectric barrier discharge (DDBD) plasma was applied to the reaction system in situ to remove the excessive surface N, which yields a pronounced improvement of the catalytic performance. The work demonstrates that hidden active phase in thermal catalysis can be unfolded when the rate-determining step is subdued by applied plasma.

1. Introduction

As a hydrogen carrier, ammonia (NH_3) can be easily liquefied, purified and transported [1,2]. Therefore, attractive application prospect of NH_3 in hydrogen fuel cell is foreseen since ultrapure CO-free hydrogen can be produced through its decomposition [3–6]. As the inverse reaction of NH_3 synthesis, NH_3 decomposition has been extensively studied [2–9]. High efficient catalysts for NH_3 synthesis such as Ni, Fe, Ru, Mo and their alloys usually show also good catalytic performance for its decomposition [10–18], although "the optimal catalyst for ammonia synthesis is never optimal for NH_3 decomposition" [19,20]. This phenomenon results essentially from the reaction kinetics determined by the two elementary reaction steps with competing activation barriers: the initial dehydrogenation of the adsorbed NH_3 and the recombination desorption of surface nitrogen (N) atoms [20–22]. Ganley et al. has proposed a theoretical correlation between the rate of NH_3 decomposition and the N-H bond scission and N-N recombination [21], showing that the decomposition rate over Fe, Co, Ni are limited by N-N recombination, while over other metals like Ru, Ir, Pd, Pt, Cu by N-H bond scission. The fact that Ru exhibits the best catalytic performance

for NH_3 decomposition is possibly the result of the good balance between these two competing steps [11,23–25]. Stronger metal-nitrogen bond (M-N) facilitates the scission of NH_x bond, but is generally accompanied with higher barrier for N-N recombination, and vice versa [26]. For the iron catalysts, the high N-N recombination barrier leads to nitridation of the catalysts during reaction [27,28]. The result of nitridation, however, is not necessarily negative for the catalysts since some iron nitride phases were reported to show even better catalytic performance than pure Fe, although the reported active phases were quite divergent and even competing [9,29–35]. Nevertheless, valuable information in safety can be deduced: the iron catalyst will be poisoned with deep nitridation, and reducing surface N atoms may promote the catalytic activity toward NH_3 decomposition [33,36,37]. Indeed, both nitridation and decomposition of iron nitrides occur simultaneously during the reaction and finally reach different equilibrium states, depending on the reaction temperature and space velocity adopted in the experiment [38]. This means the phase of catalyst during and after a reaction could be just an indication of the final stable phase, and may not represent the most active phase. How to discover and keep the potential most active phase would be of great interest for the development of

* Corresponding authors.
  E-mail addresses: wangxuan@zzu.edu.cn (X. Wang), hsqiu@zzu.edu.cn (H. Qiu).

iron-based catalysts. To this end, real-time tracking on the whole reaction process as well as the structure evolution of the catalysts would be one of the choices.

In this work, NH_3 decomposition over iron catalyst was monitored in situ with a mass spectrometer (MS) based microreactor. An evanescent active phase uniquely for dehydrogenation of NH_3 was uncovered at a Fe/Fe_4N mixing phase prior to gradual deactivation. Density functional theory (DFT) calculations revealed that deposition of an N atom on Fe (100) can significantly reduce the dehydrogenation barrier over the surrounding iron atoms. Ambient-pressure double dielectric barrier discharge (DDBD) plasma with appropriate power was applied to the reaction system, which notably lowers down the apparent reaction barrier and realizes a low-temperature application.

2. Experimental section

2.1. Apparatus

The MS based microreactor consists of a π-shape quartz reactor (outer diameter of 8 mm and inner diameter of 6 mm) and a coaxial quartz tube (outer diameter of 3 mm and inner diameter of 1 mm) (Fig. S1). A piece of stainless steel foil was wrapped around the middle region of the π-shape reactor. Heating coil was then tightly wound outside the foil. A K-type thermocouple wire was placed under stainless steel foil to measure the temperature of sample, which may lead to 10–15 K higher than that measured directly inside the tube. A copper rod was placed in the inner tube and connected to the high voltage end of a plasma generator (0–30 kV, 5–25 kHz). The gas flow was controlled by a mass flow controller (MFC, 0–100 standard cubic centimeter per minute (SCCM)). The tail gas can be analyzed by a real-time mass spectrometer (MS, Pfeiffer, QMG 220).

2.2. Sample preparation

Equal weight of commercial Fe_2O_3 (the specific surface area of 2.5 m^2/g) and MgO powder mixture was milled for 20 min (min). The mixture (160 mg) was then packed in the reactor. Before reaction the Fe_2O_3/MgO catalyst was oxidized in O_2 flow (50 SCCM) at 800 K for 30 min to remove possible contaminations and then reduced in H_2 flow (50 SCCM) at 950 K for 10 min

2.3. Temperature Programmed Surface Reactions (TPSR)

After reduction, the Fe/MgO sample was heated linearly in 5% NH_3/Ar flow (50 SCCM) from room temperature (RT) to the target temperature (0.5 K/s). For a repeated cycle of experiment, the sample was cooled down to RT in the flow prior to the next temperature ramp process.

2.4. XRD

Powder X-ray diffraction (XRD) pattern of the samples were acquired on a Bruker D8 ADVANCE with Cu-Kα radiation (λ = 1.5418 Å). The different reaction stages of the catalyst were controlled by time under the same reaction condition.

2.5. In situ Double Dielectric Barrier Discharge (DDBD) Plasma

The in situ DDBD plasma was realized by applied a high voltage (e.g., 3–12 kV, 10 kHz) on the copper rod with the stainless steel foil either grounded or connected to the sampling port on the plasma generator (Fig. S1). The input power was obtained by multiplying the voltage with the current shown on the plasma generator. The power of plasma was monitored by a digital oscilloscope (Fig. S2).

2.6. DFT calculations

Density functional theory (DFT) calculations were performed with the Vienna Ab initio Simulation Package (VASP) [39]. The generalized gradient approximation (GGA) has been utilized in all calculations based on the specific functional of Perdew-Burke-Ernzerhof (PBE) [40–42]. The Fe(100) surface was modeled by a (5 × 5) supercell slab with four iron layers [43]. A vacuum layer of 15 Å above the surface was created to avoid periodic interaction along Z-direction. 2 × 2 × 1 Monkhorts-Pack mesh of k-points was applied on the Brillouin zone. The cutoff kinetic energy for the plane wave basis set was 450 eV, with the force and energy convergence criterion of 0.01 eV/Å and 10^{-5} eV respectively. Transition states were searched by climbing image nudged elastic-band (CI-NEB) method [44] and the dimer method [45]. All calculated energies have been corrected with zero point energy (ZPE). The Bader charge distribution was analyzed by Visual Molecular Dynamics (VMD).

3. Results and discussion

3.1. Hidden active phase for dehydrogenation of NH_3

Fig. 1 presents the real-time monitoring of NH_3 decomposition over iron catalyst at three specified temperatures (700 K, 780 K and 880 K). Results of lower and higher temperature were not shown because the initial decomposition of NH_3 over iron catalyst occurs at about 670 K (Fig. S3) and NH_3 may decompose in gas phase at higher temperature
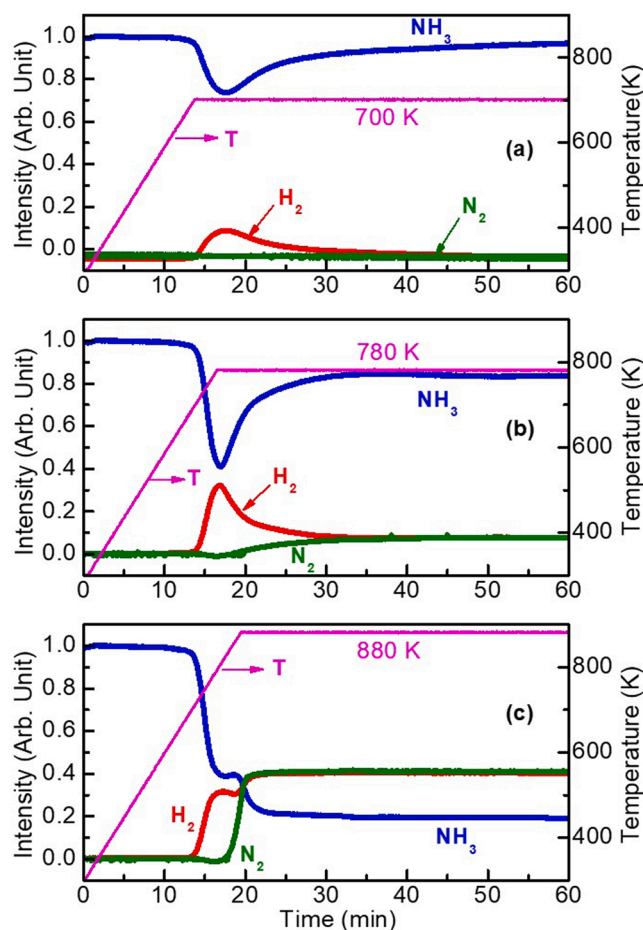

Fig. 1. Real-time monitoring of NH_3 decomposition over Fe/MgO catalyst at specified temperature. The heating rate was 0.5 K/s. Gas: 5% NH_3/Ar and 50 SCCM. Weight of catalyst: 160 mg. The pink lines marked with T correspond to the right axis denoting the temperature ramp and holding process.

(Fig. S4). At 700 K, the decomposition rate of NH$_3$ gradually reaches a maximum at a flex point and then declines slowly to a constant value that is slightly lower than that of the incoming flow rate (note that the ion current in MS is proportional to the concentration of gas in the flow, as well as to the decomposition rate). The initial acceleration of the decomposition rate indicates a self-acceleration of the catalyst in dehydrogenation activity. We therefore name the flex point as "critical point" that represents the state of catalyst corresponding to the maximum dehydrogenation rate. It is worth noting that no N$_2$ is released in the whole process for the experiment performed at 700 K, which indicates that all N atoms from decomposed NH$_3$ are accumulated on the iron catalyst. Herein, the accumulation of N exhibits both positive (e.g., the initial activation before the critical point) and negative (e.g., the following deactivation after the critical point) effect on the catalytic performance of iron catalyst, in line with the previous work [36,37]. At 780 K (Fig. 1(b)), the NH$_3$ and H$_2$ curves show similar characters except for a gradually increase of N$_2$ desorption and higher conversion rate of NH$_3$ at stable state. Indeed, the accumulation of N will continue till the reaction reaches a stable state (e.g., after 40 min). In other words, the final state of the catalyst, which determines reaction kinetics, is in turn influenced by reaction parameters (e.g., temperature, pressure and space velocity). In Fig. 1(c), elevating the reaction temperature to 880 K significantly shortens the time to stabilize the reaction and elevates the NH$_3$ conversion rate at stable state (83%). The flex at about 15 min is essentially of the same origin with the ones present at low temperature corresponding to an activation-deactivation process toward dehydrogenation activity. Indeed, from a traditional point of view, such process is not considered catalytic, but an activation process in that either the catalyst or reaction was changing (in a short time scale). The evanescent phase at critical point therefore is thought to be a hidden active phase

uniquely toward dehydrogenation of NH$_3$.

Fig. 2(a) shows XPS spectra of Fe$_x$N after the samples were sputtered for the indicated time. The Fe 2p peaks of as prepared samples reveal a feature of iron oxides, revealing that the samples were oxidized possibly during the exposure to air. The presence of FexN is seen after the sample was sputtered 0.5 hours (h), but the oxide was fully removed after 2-hour sputtering. Fig. 2(b) and (c) present the Fe 2p and N 1 s spectra of the Fe/MgO catalysts at different reaction stages indicated by the point in the inset of Fig. 2(b) (after 5-hour sputtering). From point/curve A to E, the Fe 2p peaks shift to higher binding energy, in line with the expectation that more electrons would be transferred to nitrogen atom for deeper nitridation. Peak fitting was not carried out since the binding energy of Fe 2p are close each other. Quantitative analysis based on the peak fitting results is therefore relatively arbitrary and unreliable. The peak intensity of N 1 s gradually increases from point/curve A to E, indicating a gradual nitridation process during the reaction.

3.2. Structure-activity relationship

To explore the structure-activity relationship of the iron catalyst, in Fig. 3, several Fe/MgO catalysts at different nitridation stages (indicated by the points on the inset curve) were characterized by XRD. As shown by the point/curve A, the catalyst after reduction exhibits a pure iron phase. The point B, which corresponds to a maximum dehydrogenation rate, is represented by a Fe/Fe$_4$N mixing phase. After point B, the iron catalyst becomes gradually deactivated accompanied with the absence of pure iron phase and the presence of Fe$_3$N (point/curve C). From Point C to E, the catalyst experiences a gradual deeper nitridation to the final Fe$_2$N phase, during which the catalyst has little change in the low dehydrogenation activity. The dehydrogenation activity, by the
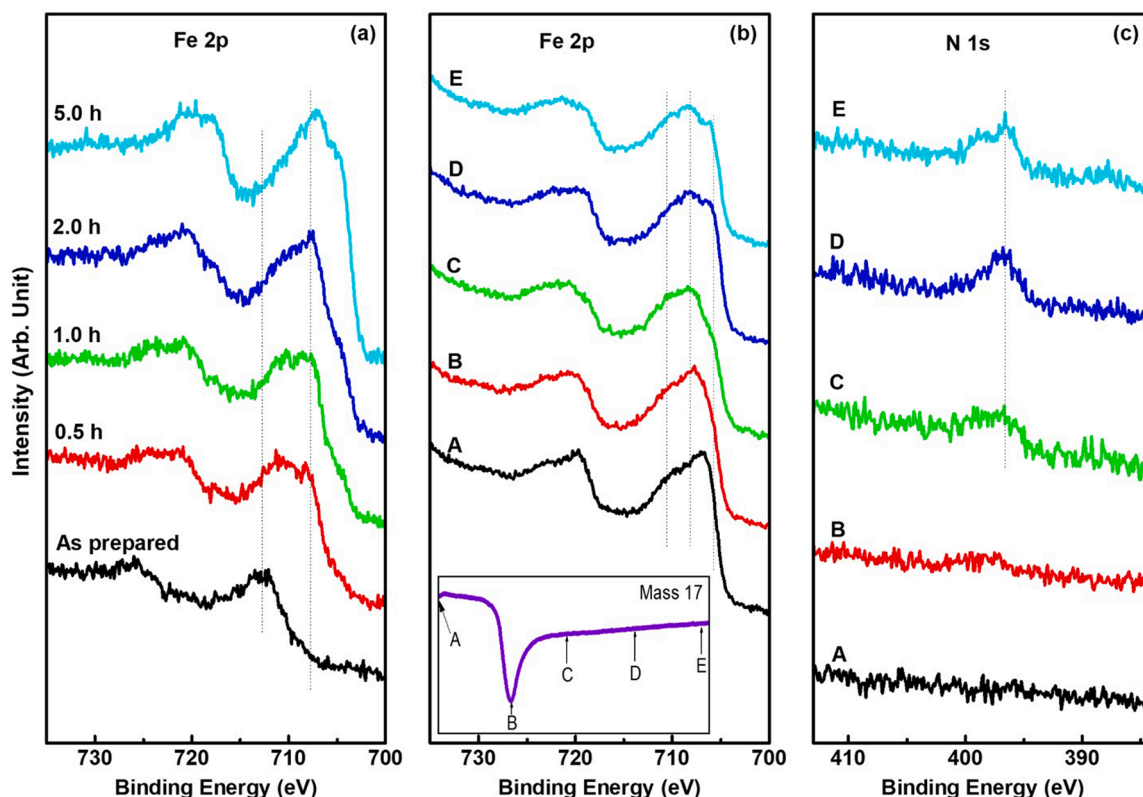

Fig. 2. XPS spectra of the Fe/MgO catalysts at different reaction stages. (a) The fully nitridized sample at 700 K (for 1 h) was sputtered for the indicated time. Fe 2p (b) and N 1 s (c) characterization after 5-hour sputtering of the Fe/MgO catalysts at different reaction stages. The reaction stage was controlled by reaction time and represented by the symbols A–E in the inset of (b). Reaction parameters: 5% NH$_3$/Ar and 50 SCCM@ 700 K. Weight of catalyst: 160 mg. The anode adopted in XPS was aluminum. The argon (Ar) ion sputtering parameters: 1 kV and 1×10^{-5} mbar Ar. The binding energies were calibrated according to the contaminant carbon species.
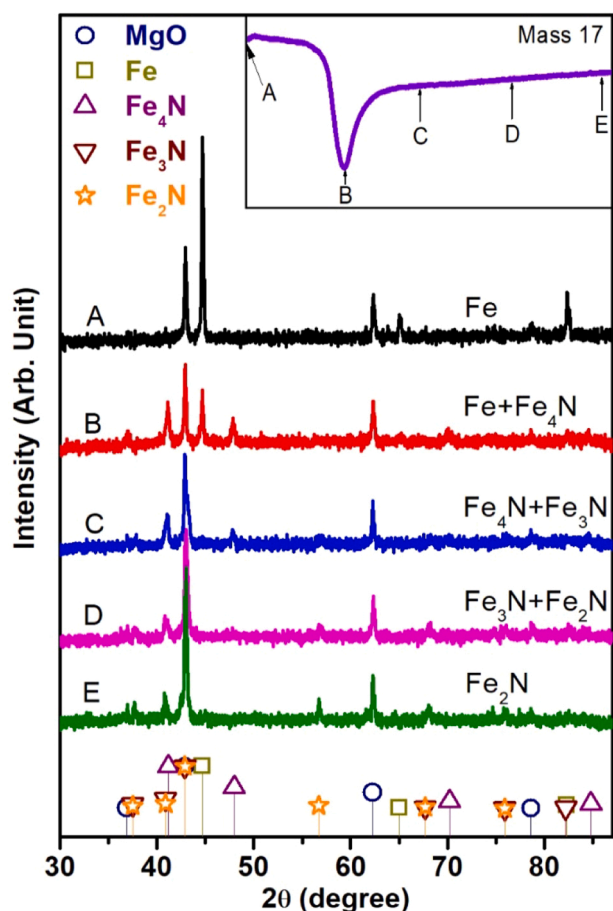
Fig. 3. XRD patterns of the iron catalyst at different reaction stages during NH_3 decomposition at 700 K. The reaction stage was controlled by reaction time and represented by the symbols A–E in the inset. The diffraction peaks of possible materials according to the standard PDF card (MgO: 71–1176; Fe: 99–0064; Fe_4N: 83–0875; Fe_3N: 72–2125; Fe_2N: 73–2102) were labeled at the bottom.

Fig. 4. NH_3 conversion rate as a function of the total N content (molar ratio of N to iron) in iron catalyst at specified temperature. The absolute N content was calculated by the molar difference between produced N_2 and H_2, e.g., in Fig. 2. See Fig. S5 and discussion for more details.

3.3. Role of initial nitridation

DFT calculations have been performed on the (100) surface of a (5 × 5 × 4) iron slab to understand the origin of the critical point since Fe_4N (100) is the most stable surface on which the arrangement and inter-distance of irons are similar to that of Fe(100) (Fig. S6). The influence of nitridation of iron on adsorption ability and the energy barrier of initial dehydrogenation was investigated. Fig. 5(a) shows the optimized geometry of N adsorbed on Fe(100) surface. The N was partially inlaid in the four-fold hollow site (about 0.4 Å above the surface) with a binding energy of 1.71 electronvolt (eV). The four iron atoms surrounding N are slightly deviated from the lattice position and shrunk towards the centered N. The Bader charge distribution of the system is shown in

combination of XRD results and activity test, is likely correlated uniquely with the Fe/Fe_4N mixing phase since both the pure Fe (point A) and Fe_4N phase (point C) correspond to notably low dehydrogenation activity. Indeed, as the XRD results give less quantitative information, the Fe/Fe_4N mixing phase may represent a wide range of Fe to Fe_4N ratio, which is discrepant from the narrow flex at critical point. Quantitative information will be beneficial to the issue.

In Fig. 4, NH_3 conversion rate was plotted versus the total N content on catalyst (the molar ratio of accumulated N to iron) at varied temperatures (Fig. S5 and discussion). The curves straightforwardly demonstrate the correlation between decomposition rate and nitridation levels of the iron catalyst. Maximum NH_3 decomposition rate corresponds to an N content of 6–12% for each different temperature. The varied total N content originates from the diffusion equilibrium between surface and bulk N at different temperature. Thus, the coverage of N on catalyst surface could be different from the value of total N content (this will be discussed in the following text). In addition, the curves in Fig. 4 are ended at different N content because the recombination barrier of surface N decreases at higher coverage and finally the catalyst is stabilized at a specific state depending on the nitridation-desorption equilibrium. For the same reason, the higher conversion rate at higher temperature would be also contributed by the relatively lower content of accumulated N. In other words, high temperature (e.g., 880 K and higher) is needed to get the iron catalyst more active, which seems a paradox per se.
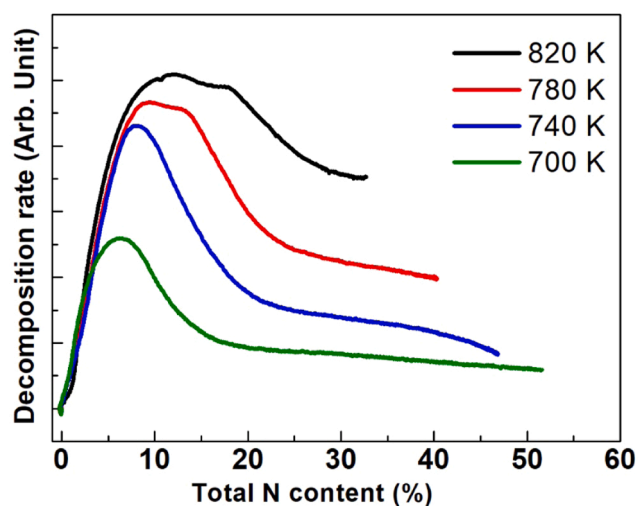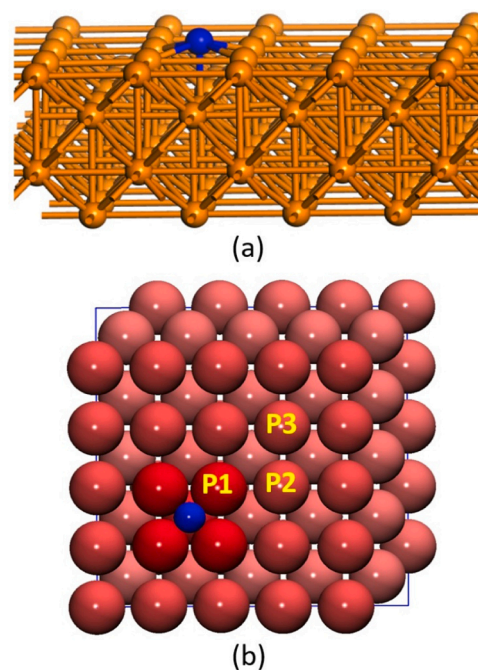

Fig. 5. (a) the optimized geometry of N adsorbed on Fe(100) surface; (b) the Bader charge distribution in (a) with the charge number discriminated by colors. For both panels, the blue sphere denotes N, others are Fe.

Fig. 5(b) with the charge number discriminated by color. The Bader charge of the N is 6.19e and of the iron atoms labeled P1, P2, and P3 are 7.72e, 7.94e, 7.95e, respectively, indicating a transfer of electron from iron to the N atom. For this account, the adsorption energy (E_{ads}) and energy barrier for the initial dehydrogenation (ΔE_1) of NH_3 on clean Fe (100) and over position P1, P2 and P3 shown in Fig. 5(b) was further investigated. The E_{ads} and ΔE_1, along with initial state, transition state and final state, are summarized in Table 1. On both clean and N deposited Fe(100) surfaces, NH_3 bonds to the surfaces via the N atom. The E_{ads} is only slightly changed upon the deposition of N. By contrast, ΔE_1 on position P1 significantly decreases relative to that on clean surface, which would cause an abrupt increase in dehydrogenation activity. We speculate that the decrease of ΔE_1 on P1 originates from either the modification of electronic structure of iron by deposited N (through charge transfer and possibly the shift of D-band center) or the repulsion between deposited N and adsorbed NH_3 that pushes the NH_3 in a tilted geometry facilitating the bonding between H and neighbored iron.

Indeed, several attempts to titrate the coverage of surface N (e.g., with NH_3, CO, O_2) at critical point have failed because the adsorption ability to the titration gas has been changed after N deposition. A very rough estimation may come from the fact that very divergent results were obtained on small slab (e.g., 2×2 and 3×3) due to the repulsion between adsorbed NH_3 molecules, and the results got converged when the slab was larger than (4×4). Therefore, the coverage of surface N at critical point was estimated to be a small value, e.g., of around 1/16.

3.4. Recovery of the hidden active phase

As the relevant product of NH_3 decomposition is hydrogen, the dehydrogenation rate is of more interest for the design of catalysts, which is indeed correlated with exploring the hidden active phase (critical point) for the iron catalyst. To this end, ambient-pressure double dielectric barrier discharge (DDBD) plasma with different power was applied in situ to the system (Fig. S1). In Fig. 6(a), when the reaction reached a stable state at 820 K (indicated by the vertical dash line), DDBD plasma with different power was applied to the system. The applied voltages were specified in the figure with the unit of kilovolt and the frequency was 10 kHz. With increasing the applied voltage, the
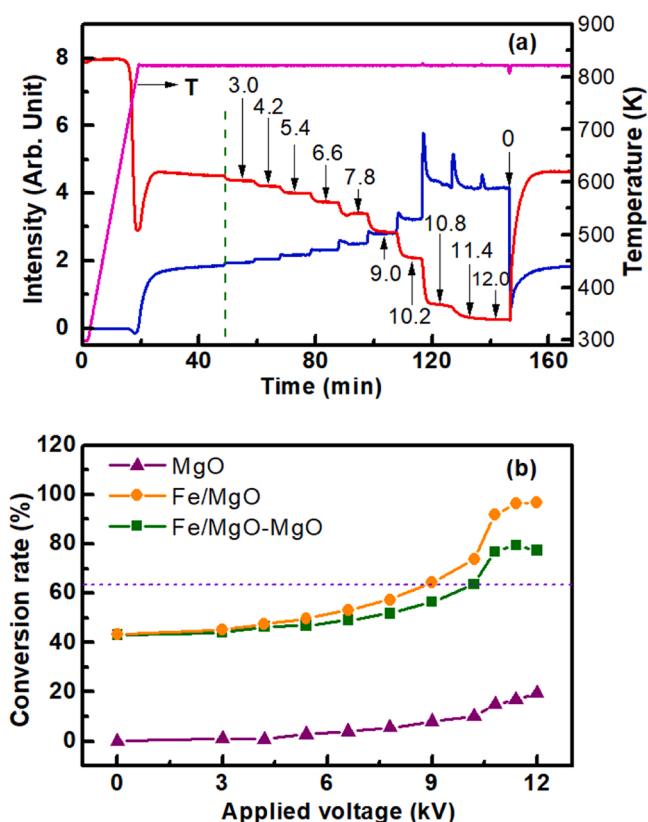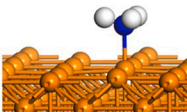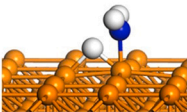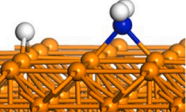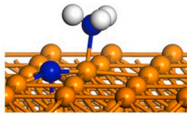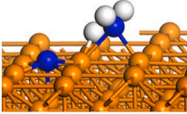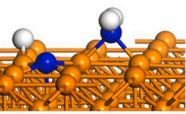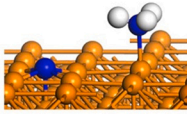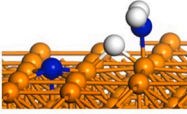

Fig. 6. (a) Real-time monitoring of NH_3 decomposition over Fe/MgO catalyst at 820 K followed by DDBD plasma with indicated voltages in kilovolt. The frequency of the high voltage was 10 kHz. The curve of H_2 was closely correlated with the change of NH_3 and therefore not shown. (b) The conversion rate as function with applied voltages on Fe/MgO, pure MgO (with the sa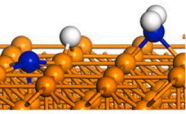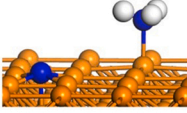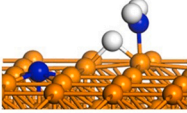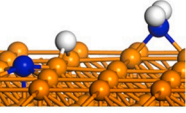me weight as was adopted in Fe/MgO) and their difference (labelled as Fe/MgO-MgO). The dash line indicates the conversion rate of NH_3 at the critical point in (a).

Table 1

Summarized initial states, transition states, final states, adsorption energies (E_{ads}) and initial dehydrogenation barrier (ΔE_1) of NH_3 adsorbed on clean Fe(100) and on P1, P2, P3 positions labelled in Fig. 5(b). The unit of energies is in eV.

Position	Initial state	Transition state	Final state	E_b	ΔE
Clean Fe(100)				0.6313	0.9034
P1				0.5403	0.5910
P2				0.6420	0.9041
P3				0.6079	0.9170

decomposition rate gradually increases, as the result of partially removing surface N (see the N_2 pulse at the beginning of each voltage). For the applied voltage of 9 kV, the dehydrogenation rate reaches the same level with the critical point and the plasma power was calculated to be 2.9 watts (W) (Table S1). A final conversion rate of 96.7% was obtained with the input voltage of 12 kV and the plasma power of 10.1 W. After the high voltage was removed at about 145 min, the decomposition rate of NH_3 decreases rapidly to the level of the stable state before applying high voltage. The rapid change could be an indication that surface N plays a key role in determining the dehydrogenation activity of the iron catalyst. The speculation is in line with the XRD results (Fig. S7) that in situ plasma treatment at high temperature leads negligible change in either the bulk structure or particle size (as indicated by the position, intensity and width of the diffraction peaks), although plasma treatment at RT refines the particle to some extent.

To investigate the possible influence of plasma effect on gas and support material, a blank experiment was performed on MgO with the same reaction condition as was performed in Fig. 6(a). The conversion rate of NH_3 over Fe/MgO and MgO, as well as their difference were plotted in Fig. 6(b). The horizontal dash line indicates the conversion rate at the critical point corresponding to an ideal highest thermal decomposition rate over the catalyst at 820 K. With no voltage applied, the MgO does not show any activity for NH_3 decomposition at 820 K. The decomposition of NH_3 under high voltage comes from the gas phase decomposition induced by plasma, which contributes less than 20% to the total decomposition of NH_3 over Fe/MgO catalyst. By subtracting the contribution of gas and support, the differential curve (the green curve decorated with solid-square) denotes the pure thermal and plasma effect on iron (intrinsic activity). The curve crosses with the dash line at about 10.2 kV that is the voltage to recover the catalyst to the critical point. However, the conversion rate increases even higher than that of the critical point with higher voltages. We speculate that it could be originated from the synergetic effect through the adsorption of excited molecule (undecomposed) on the catalyst surface. In this case, the critical point of the catalyst emerges when applied a voltage of 11.4 kV, because the intrinsic activity (indicated by the Fe/MgO-MgO curve) starts to decrease with higher voltage.

The enhancement of catalytic performance with plasma can be attributed to the following three factors: (1) the gas phase decomposition under plasma; (2) the enhancement due to the adsorption and reaction of excited molecules on catalyst surface; (3) the enhancement of the thermal catalytic performance due to the recovery of the hidden active phase. In this case, although the energy of plasma was injected into the reaction system to overcome the N-N recombination barrier, the improvement of catalytic performance was also (mainly) contributed by the hidden active phase. Therefore, overall, less energy was required to overcome the apparent kinetic barrier.

In a general sense, a catalytic reaction usually contains several elemental steps, of which the best catalyst is thought to uniquely reduce the energy barrier of rate determining step or to show the best statistical performance for all steps. In other words, a catalyst would not catalyze each elemental step of a reaction. In the case that the rate determining step may be "catalyzed" by plasma, the best catalyst for plasma catalysis would deviate from the one for thermal catalysis. Microscopic understanding of the reaction and the plasma effect must be gained to realize a rational design of the catalyst under plasma.

4. Conclusions

The nitridation of iron catalyst during NH_3 decomposition renders a significant change in its phase and catalytic properties. A hidden active phase for the initial dehydrogenation was determined to be a Fe/Fe_4N mixing phase of which the N atoms modify the electronic structure of their surrounding irons, leading to an abrupt reduction of the dehydrogenation barrier. As DDBD plasma can efficiently remove the surface N, the hidden (thermally) active phase was recovered under in situ plasma condition, which significantly improve the catalytic performance and realizes a low-temperature application.

While people habitually pay more attentions on the stable state of catalytic reactions, the activation process may provide more elemental details about the reaction mechanism. The present work, on one hand, discovers a hidden active phase over iron catalyst for ammonia decomposition; on the other hand, demonstrates a novel idea for the research of plasma catalysis. In the future, this method will be applied to catalyst system that has stronger N binding energy and smaller H scissoring barrier.

CRediT authorship contribution statement

Bin Lu: Investigation, Writing – original draft. **Ling Li**: DFT calculations. **Menghao Ren**: Investigation. **Yu Liu**: Methodology. **Yanmin Zhang**: Methodology. **Xin Xu**: Methodology. **Xuan Wang**: Writing – review & editing. **Hengshan Qi**u: Supervision, Funding acquisition, Writing – review & editing.

Declaration of Competing Interest

The authors declare that they have no known competing financial interests or personal relationships that could have appeared to influence the work reported in this paper.

Acknowledgements

Appendix A. Supporting information

Supplementary data associated with this article can be found in the online version at doi:10.1016/j.apcatb.2022.121475.

References

[1] K.E. Lamb, M.D. Dolan, D.F. Kennedy, Ammonia for hydrogen storage; a review of catalytic ammonia decomposition and hydrogen separation and purification, Int. J. Hydrog. Energy 44 (2019) 3580–3593.
[2] A. Takahashi, T. Fujitani, Kinetic analysis of decomposition of ammonia over nickel and ruthenium catalysts, J. Chem. Eng. Jpn. 49 (2016) 22–28.
[3] T.V. Choudhary, C. Sivadinarayana, D.W. Goodman, Catalytic ammonia decomposition: COx-free hydrogen production for fuel cell applications, Catal. Lett. 72 (2001) 197–201.
[4] F. Schüth, R. Palkovits, R. Schlögl, D.S. Su, Ammonia as a possible element in an energy infrastructure: catalysts for ammonia decomposition, Energy Environ. Sci. 5 (2012) 6278–6289.
[5] T.A. Le, Y. Kim, H.W. Kim, S.U. Lee, J.R. Kim, T.W. Kim, Y.J. Lee, H.J. Chae, Ru-supported lanthania-ceria composite as an efficient catalyst for COx-free H-2 production from ammonia decomposition, Appl. Catal. B-Environ. 285 (2021) 11.
[6] S. Mukherjee, S.V. Devaguptapu, A. Sviripa, C.R.F. Lund, G. Wu, Low-temperature ammonia decomposition catalysts for hydrogen generation, Appl. Catal. B-Environ. 226 (2018) 162–181.
[7] Ö. Akarçay, S.F. Kurtoğlu, A. Uzun, Ammonia decomposition on a highly-dispersed carbon-embedded iron catalyst derived from Fe-BTC: Stable and high performance at relatively low temperatures, Int. J. Hydrog. Energy 45 (2020) 28664–28681.
[8] C. Chen, Y. Chen, A.M. Ali, W. Luo, J. Wen, L. Zhang, H. Zhang, Bimetallic Ru-Fe nanoparticles supported on carbon nanotubes for ammonia decomposition and synthesis, Chem. Eng. Technol. 43 (2020) 719–730.
[9] W. Arabczyk, J. Zamlynny, Study of the ammonia decomposition over iron catalysts, Catal. Lett. 60 (1999) 167–171.
[10] S.-F. Yin, Q.-H. Zhang, B.-Q. Xu, W.-X. Zhu, C.-F. Ng, C.-T. Au, Investigation on the catalysis of COx-free hydrogen generation from ammonia, J. Catal. 224 (2004) 384–396.
[11] D.A. Hansgen, D.G. Vlachos, J.G. Chen, Using first principles to predict bimetallic catalysts for the ammonia decomposition reaction, Nat. Chem. 2 (2010) 484.
[12] J. Zhang, H. Xu, X. Jin, Q. Ge, W. Li, Characterizations and activities of the nano-sized Ni/Al2O3 and Ni/La–Al2O3 catalysts for NH3 decomposition, Appl. Catal. A: Gen. 290 (2005) 87–96.

[13] A.M. Karim, V. Prasad, G. Mpourmpakis, W.W. Lonergan, A.I. Frenkel, J.G. Chen, D.G. Vlachos, Correlating particle size and shape of supported Ru/γ-Al2O3 catalysts with NH3 decomposition activity, J. Am. Chem. Soc. 131 (2009) 12230–12239.

[14] P. Xie, Y. Yao, Z. Huang, Z. Liu, J. Zhang, T. Li, G. Wang, R. Shahbazian-Yassar, L. Hu, C. Wang, Highly efficient decomposition of ammonia using high-entropy alloy catalysts, Nat. Commun. 10 (2019) 4011.

[15] T. Kocer, F.E. Sarac-Oztuna, S.F. Kurtoglu-Oztulum, U. Unal, A. Uzun, Effect of nickel precursor on the catalytic performance of graphene aerogel-supported nickel nanoparticles for the production of COx-free hydrogen by ammonia decomposition, Energy Technol. 10 (3) (2022), 2100794, https://doi.org/10.1002/ente.202100794.

[16] M. El-Shafie, S. Kambara, Y. Hayakawa, Energy and exergy analysis of hydrogen production from ammonia decomposition systems using non-thermal plasma, Int. J. Hydrog. Energy 46 (2021) 29361–29375.

[17] K. Yuan, P. Hao, X. Li, Y. Zhou, J. Zhang, S. Zhong, First-principles insights into ammonia decomposition on the MoN(0001) surface, N. J. Chem. 45 (2021) 15234–15239.

[18] A. Srifa, K. Okura, T. Okanishi, H. Muroyama, T. Matsui, K. Eguchi, Hydrogen production by ammonia decomposition over Cs-modified Co3Mo3N catalysts, Appl. Catal. B-Environ. 218 (2017) 1–8.

[19] A. Boisen, S. Dahl, J.K. Norskov, C.H. Christensen, Why the optimal ammonia synthesis catalyst is not the optimal ammonia decomposition catalyst, J. Catal. 230 (2005) 309–312.

[20] X. Zhang, Z. Lu, D. Ma, Z. Yang, Adsorption and dissociation of ammonia on small iron clusters, Int. J. Hydrog. Energy 40 (2015) 346–352.

[21] J.C. Ganley, F.S. Thomas, E.G. Seebauer, R.I. Masel, A priori catalytic activity correlations: the difficult case of hydrogen production from ammonia, Catal. Lett. 96 (2004) 117–122.

[22] G. Lanzani, K. Laasonen, NH3 adsorption and dissociation on a nanosized iron cluster, Int. J. Hydrog. Energy 35 (2010) 6571–6577.

[23] X.C. Hu, X.P. Fu, W.W. Wang, X. Wang, K. Wu, R. Si, C. Ma, C.J. Jia, C.H. Yan, Ceria-supported ruthenium clusters transforming from isolated single atoms for hydrogen production via decomposition of ammonia, Appl. Catal. B-Environ. 268 (2020) 13.

[24] X.H. Ju, L. Liu, P. Yu, J.P. Guo, X.L. Zhang, T. He, G.T. Wu, P. Chen, Mesoporous Ru/MgO prepared by a deposition-precipitation method as highly active catalyst for producing COX-free hydrogen from ammonia decomposition, Appl. Catal. B-Environ. 211 (2017) 167–175.

[25] C. Huang, Y. Yu, J. Yang, Y. Yan, D. Wang, F. Hu, X. Wang, R. Zhang, G. Feng, Ru/La2O3 catalyst for ammonia decomposition to hydrogen, Appl. Surf. Sci. 476 (2019) 928–936.

[26] Z. Yao, A. Zhang, Y. Li, Y. Zhang, X. Cheng, C. Shi, An investigation of the thermal stability, crystal structure and catalytic properties of bulk and alumina-supported transition metal nitrides, J. Alloys Comp. 464 (2008) 488–496.

[27] J.Zy Walerian Arabczyk, Dariusz Moszyński, Kinetics of nanocrystalline iron nitriding, Pol. J. Chem. Technol. 12 (2010) 38–43.

[28] T.J. Wood, J.W. Makepeace, W.I.F. David, Neutron diffraction and gravimetric study of the iron nitriding reaction under ammonia decomposition conditions, Phys. Chem. Chem. Phys. 19 (2017) 27859–27865.

[29] R. Pelka, I. Moszyńska, W. Arabczyk, Catalytic ammonia decomposition over Fe/Fe4N, Catal. Lett. 128 (2009) 72.

[30] R. Pelka, W. Arabczyk, Studies of the kinetics of reaction between iron catalysts and ammonia—nitriding of nanocrystalline iron with parallel catalytic ammonia decomposition, Top. Catal. 52 (2009) 1506–1516.

[31] R. Pelka, K. Kiełbasa, W. Arabczyk, Catalytic ammonia decomposition during nanocrystalline iron nitriding at 475 °C with NH3/H2 mixtures of different nitriding potentials, J. Phys. Chem. C 118 (2014) 6178–6185.

[32] S.C. Yeo, S.S. Han, H.M. Lee, Mechanistic investigation of the catalytic decomposition of ammonia (NH3) on an Fe(100) surface: A DFT study, J. Phys. Chem. C 118 (2014) 5309–5316.

[33] L. Wang, Y. Zhao, C. Liu, W. Gong, H. Guo, Plasma driven ammonia decomposition on a Fe-catalyst: eliminating surface nitrogen poisoning, Chem. Commun. 49 (2013) 3787–3789.

[34] H. Zhang, Q. Gong, S. Ren, M.A. Arshid, W. Chu, C. Chen, Implication of iron nitride species to enhance the catalytic activity and stability of carbon nanotubes supported Fe catalysts for carbon-free hydrogen production via low-temperature ammonia decomposition, Catal. Sci. Technol. 8 (2018) 907–915.

[35] B. Lei, J. Wen, S. Ren, L. Zhang, H. Zhang, Highly efficient COx-free hydrogen evolution activity on rod Fe2N catalysts for ammonia decomposition, N. J. Chem. 43 (2019) 18277–18284.

[36] L. Wang, Y. Yi, Y. Zhao, R. Zhang, J. Zhang, H. Guo, NH3 decomposition for H2 generation: effects of cheap metals and supports on plasma–catalyst synergy, ACS Catal. 5 (2015) 4167–4174.

[37] T.E. Bell, L. Torrente-Murciano, H2 production via ammonia decomposition using non-noble metal catalysts: a review, Topics in Catalysis 59 (2016) 1438–1457.

[38] J.-C. Tseng, D. Gu, C. Pistidda, C. Horstmann, M. Dornheim, J. Ternieden, C. Weidenthaler, Tracking the active catalyst for iron-based ammonia decomposition by in situ synchrotron diffraction studies, ChemCatChem 10 (2018) 4465–4472.

[39] G. Kresse, J. Hafner, Ab initio molecular-dynamics for liqiud-metals, Phys. Rev. B 47 (1993) 558–561.

[40] G. Kresse, J. Furthmuller, Efficient iterative schemes for ab initio total-energy calculations using a plane-wave basis set, Phys. Rev. B 54 (1996) 11169–11186.

[41] G. Kresse, J. Furthmuller, Efficiency of ab-initio total energy calculations for metals and semiconductors using a plane-wave basis set, Comput. Mater. Sci. 6 (1996) 15–50.

[42] J.P. Perdew, K. Burke, M. Ernzerhof, Generalized gradient approximation made simple, Phys. Rev. Lett. 77 (1996) 3865–3868.

[43] V. Wang, N. Xu, J.C. Liu, G. Tang, W.T. Geng, VASPKIT: A user-friendly interface facilitating high-throughput computing and analysis using VASP code, Comput. Phys. Commun. 267 (2021), 108033.

[44] G. Henkelman, B.P. Uberuaga, H. Jonsson, A climbing image nudged elastic band method for finding saddle points and minimum energy paths, J. Chem. Phys. 113 (2000) 9901–9904.

[45] G. Henkelman, H. Jonsson, A dimer method for finding saddle points on high dimensional potential surfaces using only first derivatives, J. Chem. Phys. 111 (1999) 7010–7022.